GRAPHENE

Inducing metallicity in graphene nanoribbons via zero-mode superlattices

Daniel J. Rizzo[1,2]*, Gregory Veber[3]*, Jingwei Jiang[1,4]*, Ryan McCurdy[3], Ting Cao[1,4,5],
Christopher Bronner[1], Ting Chen[1], Steven G. Louie[1,4]†, Felix R. Fischer[3,4,6]†, Michael F. Crommie[1,4,6]†

The design and fabrication of robust metallic states in graphene nanoribbons (GNRs) are challenging because lateral quantum confinement and many-electron interactions induce electronic band gaps when graphene is patterned at nanometer length scales. Recent developments in bottom-up synthesis have enabled the design and characterization of atomically precise GNRs, but strategies for realizing GNR metallicity have been elusive. Here we demonstrate a general technique for inducing metallicity in GNRs by inserting a symmetric superlattice of zero-energy modes into otherwise semiconducting GNRs. We verify the resulting metallicity using scanning tunneling spectroscopy as well as first-principles density-functional theory and tight-binding calculations. Our results reveal that the metallic bandwidth in GNRs can be tuned over a wide range by controlling the overlap of zero-mode wave functions through intentional sublattice symmetry breaking.

Extended two-dimensional (2D) graphene is a gapless semimetal, yet when it is laterally confined to nanometer-scale 1D ribbons, a sizable energy gap emerges (*1*). Unlike carbon nanotubes (which can exhibit metallicity depending on their chirality), isolated armchair and zigzag graphene nanoribbons (GNRs) always feature a band gap that scales inversely with the width of the ribbon (*2*). This makes GNRs attractive as transistor elements for logic devices at the ultimate limits of scalability (*3*). However, it is also a limitation because metallic GNRs would be valuable as device interconnects and could create opportunities for exploring Luttinger liquids (*4*–*6*), plasmonics (*7*–*9*), charge density waves (*10*, *11*), and superconductivity (*12*, *13*) in 1D. GNRs synthesized by means of atomically precise bottom-up fabrication techniques exhibit band gaps that are in good agreement with theoretical predictions (*14*–*18*) and are thus ideal platforms for probing atomic-scale sensitivity of electronic properties in 1D structures. It has recently been shown, for example, that bottom-up synthesis can be used to place topologically protected junction states at predetermined positions along the GNR backbone (*19*–*24*) that hybridize to form the frontier GNR electronic structure. These localized states (*21*, *22*) each contribute a single unpaired electron at mid gap to the electronic structure (i.e., at E = 0), and so judicious placement of such zero-mode states raises the possibility of creating metallic and magnetic configurations. Thus far, however, only semiconducting GNRs have been fabricated with this technique (*19*, *20*).

Here we demonstrate a general approach for designing and fabricating metallic GNRs using the tools of atomically precise bottom-up synthesis. This is accomplished by embedding localized zero-mode states in a symmetric superlattice along the backbone of an otherwise semiconducting GNR. Quantum mechanical hopping of electrons between adjacent zero-mode states results in metallic bands as predicted by elementary tight-binding electronic structure models (*25*). Using scanning tunneling spectroscopy (STS) and first-principles theoretical modeling, we find that zero modes confined to only one of graphene's two sublattices (i.e., sublattice-polarized states) result in narrow-band metallic phases that reside at the border of a magnetic instability. The metallic bandwidth of these GNRs, however, can be increased by more than a factor of 20 by intentionally breaking the GNR bipartite symmetry, thus resulting in robust metallicity. This is accomplished by inducing the formation of just two new carbon-carbon bonds per GNR unit cell (each unit cell contains 94 carbon atoms in the bottom-up synthesized GNRs presented here). This marked change in electronic structure from a seemingly minor chemical bond rearrangement arises from the loss of sublattice polarization that accompanies broken bipartite symmetry. This concept provides a useful tool for controlling GNR metallicity and for tuning GNR electronic structure into different physical regimes.

Concept of GNR metallization

Our strategy for designing metallic GNRs uses a theorem based on simple nearest-neighbor tight-binding theory: A piece of graphene with a surplus of carbon atoms (ΔN) on sublattice A versus sublattice B will have a minimum of $\Delta N = N_A - N_B$ eigenstates localized on the A sublattice at $E = 0$ ("zero modes"). Here N_A (N_B) is the number of atoms residing on sublattice A (B) [see (*26*) for this theorem's derivation]. This bears resemblance to Lieb's theorem (*27*) and is also applicable to the behavior of vacancy defects in graphene (*28*–*30*). Expanding this idea to 1D GNR systems with a periodic sublattice imbalance (i.e., an imbalance in each unit cell), one can construct a low-energy effective tight-binding model to describe the resulting electronic bands by introducing a parameter, t, that represents electron hopping between adjacent localized zero modes. This concept can be used to design metallic GNRs by providing them with a unit cell that contains a surplus of two carbon atoms on sublattice A ($\Delta N = 2$). Under this construction there are two relevant hopping amplitudes: the intracell hopping amplitude (t_1) and the intercell hopping amplitude (t_2). A tight-binding analysis of this situation leads to the well-known Su-Schrieffer-Heeger (SSH) (*25*) dispersion relationship for the zero-mode bands:

$$E_{\pm}(k) = \pm\sqrt{|t_1|^2 + |t_2|^2 + 2|t_1||t_2|\cos(k+\delta)} \tag{1}$$

where δ is the relative phase between t_1 and t_2 (which, in general, can be complex numbers). Two bands result here because there are two zero-mode states per unit cell and the energy gap between them is $\Delta E = 2||t_1| - |t_2||$. If the two hopping amplitudes are identical, $|t_1| = |t_2|$, then the energy gap is reduced to zero, and the resulting 1D electronic structure should be metallic.

Synthesis of molecular precursor and sawtooth-GNRs

Using this idea as a guide for creating metallic GNRs, we designed the GNR precursor molecule **1** (Fig. 1A). A graphene honeycomb lattice superimposed onto this molecule reveals that under cyclodehydrogenation, the methyl group carbon atom attached to the central tetracene (highlighted gray in Fig. 1A) will fuse and provide one surplus carbon atom on sublattice A over sublattice B per monomer. Previous step-growth polymerizations of structurally related molecules (*20*) suggest that the surface polymerization of **1** will place the central tetracene unit in an alternating pattern on either side of the GNR growth axis. If polymerization proceeds in a head-to-tail configuration, then the resulting GNRs feature two additional carbon atoms on sublattice A per unit cell (Fig. 1A). Following cyclodehydrogenation, the anticipated GNR structure is composed of short zigzag edges

---

[1]Department of Physics, University of California, Berkeley, CA 94720, USA. [2]Department of Physics, Columbia University, New York, NY 10027, USA. [3]Department of Chemistry, University of California, Berkeley, CA 94720, USA. [4]Materials Sciences Division, Lawrence Berkeley National Laboratory, Berkeley, CA 94720, USA. [5]Department of Materials Science and Engineering, University of Washington, Seattle, WA 98195, USA. [6]Kavli Energy NanoSciences Institute at the University of California Berkeley and the Lawrence Berkeley National Laboratory, Berkeley, CA 94720, USA.
*These authors contributed equally to this work.
†Corresponding author. Email: crommie@berkeley.edu (M.F.C.); ffischer@berkeley.edu (F.R.F.); sglouie@berkeley.edu (S.G.L.)

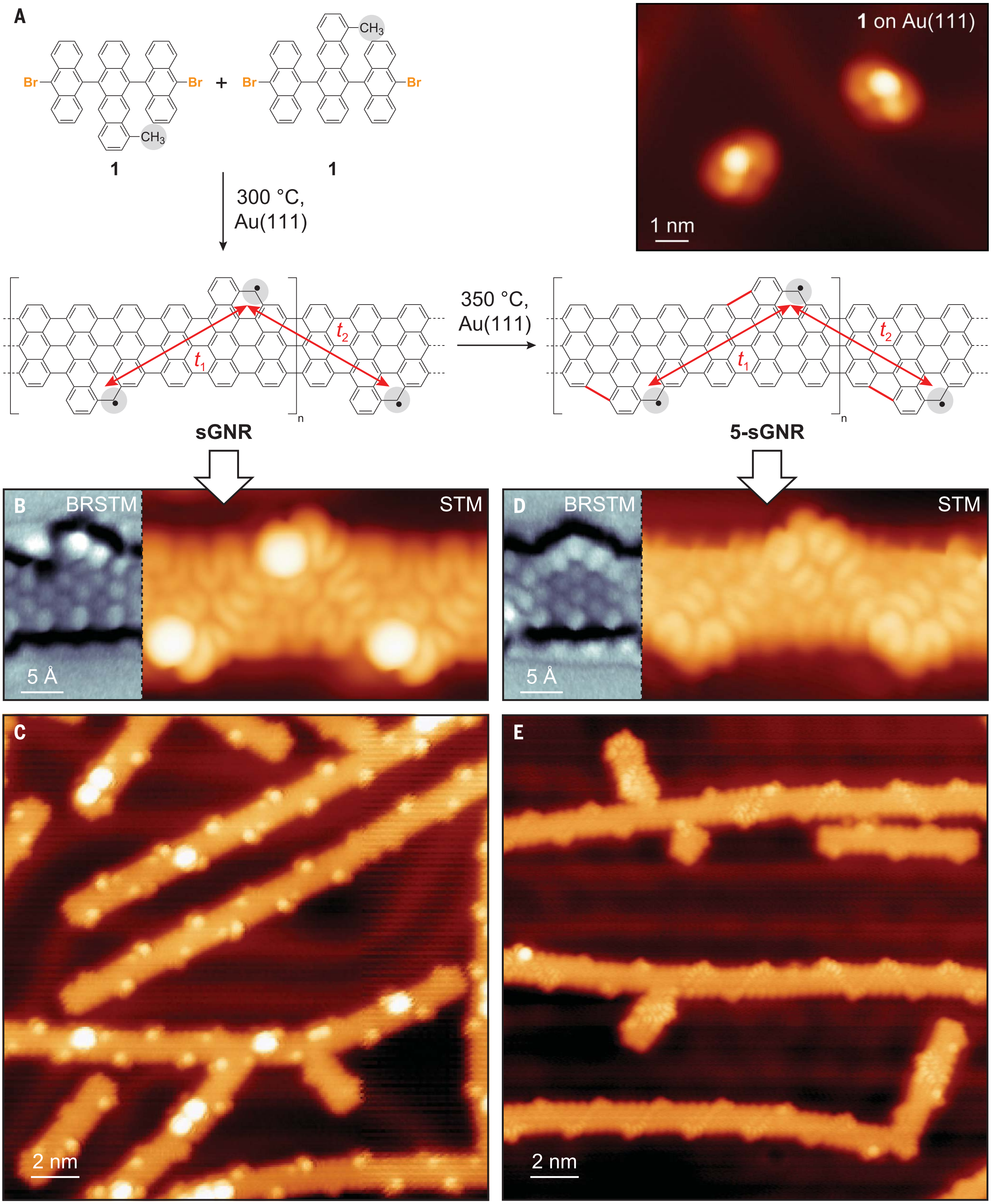

Fig. 1. Bottom-up synthesis of sawtooth-GNRs. (**A**) Schematic representation of bottom-up growth of both sGNRs and 5-sGNRs from molecular precursor **1**. Inset: STM topograph of two isolated monomers of **1** deposited on Au(111) (I_t = 30 pA, V_s = 1.000 V). (**B**) STM topograph of a segment of a sGNR (I_t = 80 pA, V_s = 0.006 V). Inset shows a bond-resolved STM (BRSTM) image of a cyclized monomer unit with an intact cove region (I_t = 110 pA, V_s = 0.010 V, V_{AC} = 10 mV). (**C**) Large-scale image of sGNRs (I_t = 30 pA, V_s = − 1.100 V). (**D**) STM topograph of a segment of a 5-sGNR (I_t = 1.5 nA, V_s = − 0.100 V). BRSTM image in inset shows how cove regions fuse to form five-membered rings (I_t = 110 pA, V_s = 0.010 V, V_{AC} = 10 mV). (**E**) Large-scale image of 5-sGNRs (I_t = 20 pA, V_s = 0.010 V).

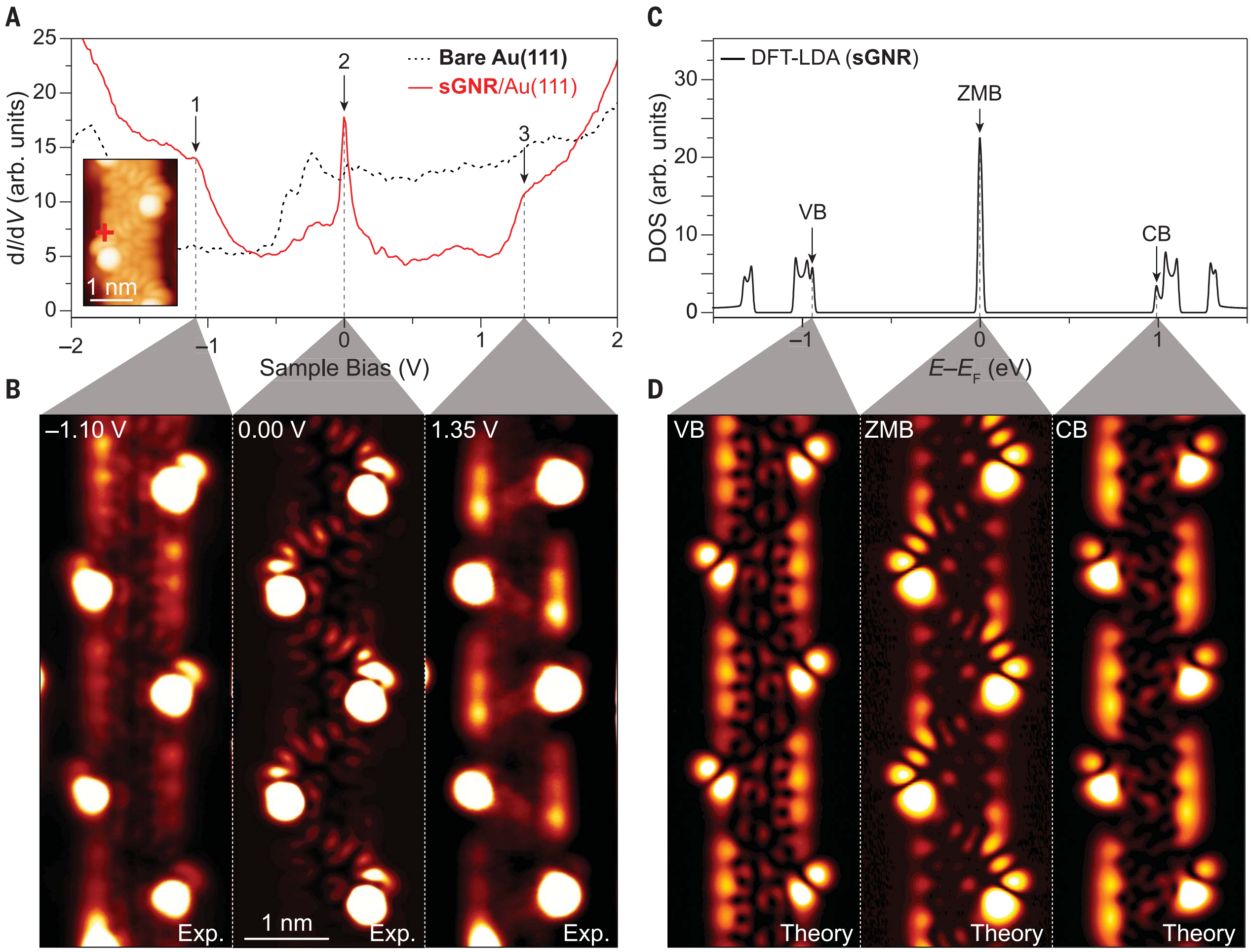

Fig. 2. Electronic structure of sGNRs. (**A**) d*I*/d*V* point spectroscopy of sGNR/Au(111) at the zigzag position marked in the inset. Dashed curve shows bare Au(111) reference spectrum (spectroscopy: V_{AC} = 10 mV; imaging: I_t = 80 pA, V_s = 0.006 V). (**B**) Constant-height d*I*/d*V* maps of sGNRs conducted at the biases indicated in (A) (spectroscopy: V_{AC} = 20 mV for states 1 and 3, V_{AC} = 4 mV for state 2). Constant-height d*I*/d*V* maps were subjected to background subtraction of substrate LDOS as described in fig. S15 (*18*, *26*). (**C**) DFT-LDA calculated DOS of the sGNR (spectrum broadened by 10-meV Gaussian). Van Hove singularities near $E - E_F = 0$ merge because of Gaussian smearing. The valence band (VB), zero-mode band (ZMB) and conduction band (CB) energies are indicated by the black arrows. (**D**) DFT-calculated LDOS of a sGNR at energies shown in (C) (LDOS sampled at a height of 3.5 Å above the plane of the sGNR) (*26*).

and prominent cove regions (reminiscent of a saw blade) and will herein be referred to as the sawtooth-GNR (sGNR). From the symmetry of the sGNR unit cell, one anticipates that the hopping amplitudes t_1 and t_2 will be equal (Fig. 1A, red arrows), resulting in a metallic band structure for the sGNR. A caveat to this approach is the limited control over head-to-tail surface polymerization, because head-to-head and tail-to-tail polymerizations place the extra carbon atoms on opposite sublattices with inequivalent hopping terms, leading to gapped semiconductors (figs. S1 and S2) (*26*). In principle, established directional solution-based polymerization techniques (*31*–*33*), as well as nascent directional on-surface polymerization strategies (*34*), could provide a route for promoting the head-to-tail structure, and hierarchical (*35*, *36*) and sterically enforced (*19*) surface growth could be used to promote head-to-head and tail-to-tail growth. Furthermore, other precursor designs should be possible that do not rely on directional growth.

Addition of (10-bromoanthracen-9-yl)lithium to a suspension of **3** followed by dehydration of crude diol precursor yielded the molecular precursor **1** for sGNRs (fig. S3) (*26*). Precursor **1** was then deposited onto a clean Au(111) surface in ultrahigh vacuum (UHV) with the use of a Knudsen cell evaporator (*26*). Figure 1A shows a representative STM image of two precursor molecules on Au(111). Step-growth polymerization of **1** was induced by heating the surface to 200°C for 20 min, followed by a second annealing step at 300°C for 20 min to complete the cyclodehydrogenation. A topographic STM image of a sGNR segment resulting from head-to-tail polymerization is depicted in Fig. 1B. Prominent periodic bright spots are observed at the locations of the cove regions owing to the nonplanar conformation induced by the superposition of hydrogen atoms (fig. S4A) (*26*). Bond-resolved STM (BRSTM) further corroborates the sGNR structure (Fig. 1B). A representative image showing the distribution of head-to-tail (Fig. 1A), head-to-head, and tail-to-tail (fig. S1) segments in the sGNR is depicted in Fig. 1C, which shows each linkage appearing in roughly equal proportions (*26*).

Prolonged annealing of sGNRs at temperatures >300°C induces a secondary cyclodehydrogenation along the cove regions that leads to the formation of five-membered rings along the edges of sGNRs (Fig. 1A). Although at 300°C this transformation remains a rare event (<30% of cove regions undergo the secondary cyclization), we were able to force the vast majority of cove regions to undergo cyclodehydrogenation by annealing to higher temperatures (~95% of cove regions undergo the secondary cyclization at 350°C). The resulting GNRs will herein be referred to as five-

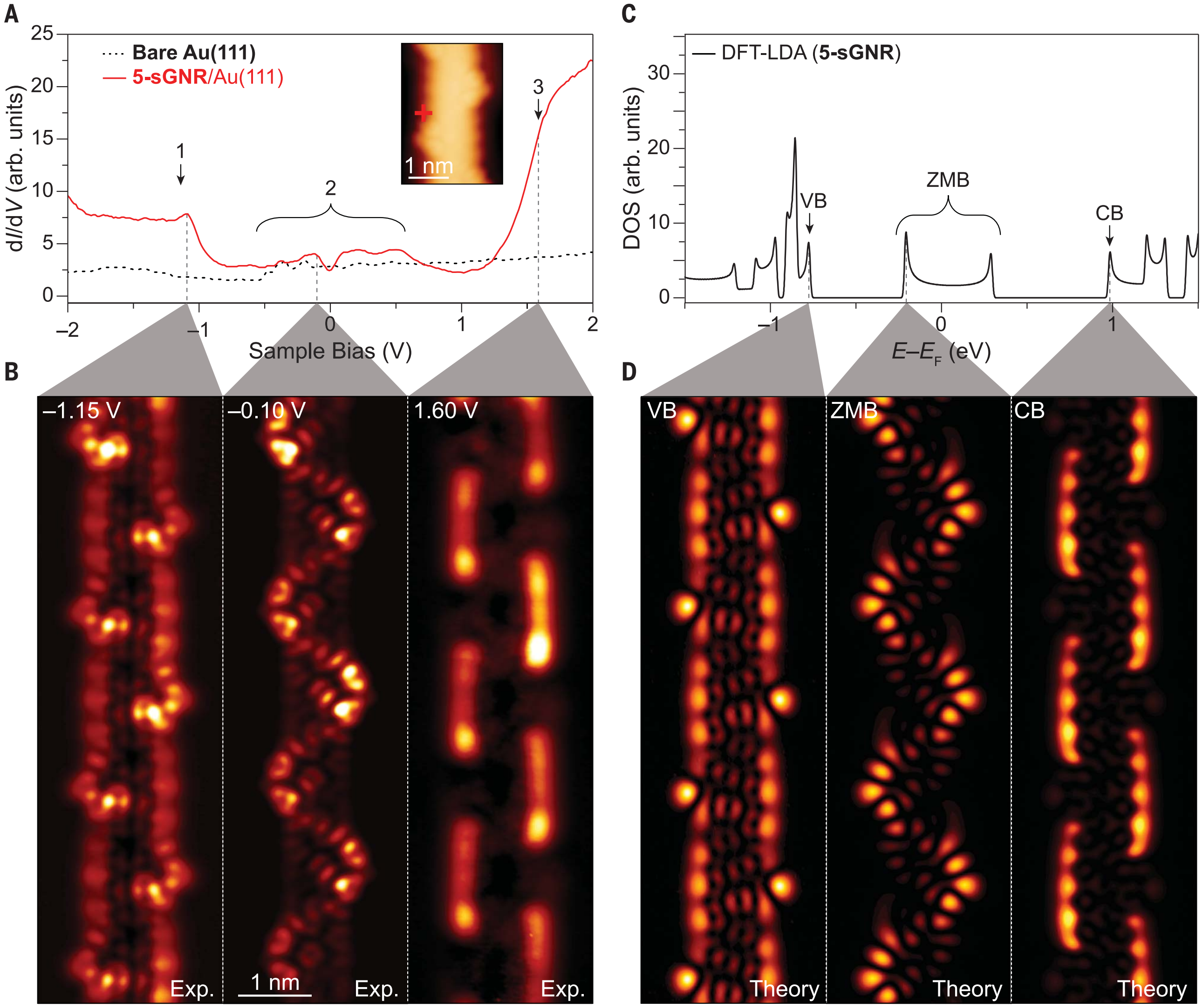

Fig. 3. Electronic structure of 5-sGNRs. (**A**) d*I*/d*V* point spectroscopy conducted on 5-sGNR/Au(111) at the zigzag position marked in the inset. Dashed curve shows bare Au(111) reference spectrum (spectroscopy: V_{AC} = 10 mV; imaging: I_t = 60 pA, V_s = – 0.100 V). (**B**) Constant-height d*I*/d*V* maps of 5-sGNRs conducted at the biases indicated in (A) (spectroscopy: V_{AC} = 20 mV). Constant-height d*I*/d*V* maps were subjected to background subtraction of substrate LDOS as described in fig. S15 (*18*, *26*). (**C**) DFT-LDA calculated DOS of the 5-sGNR (spectrum broadened by 10-meV Gaussian). The valence band (VB), zero-mode band (ZMB), and conduction band (CB) energies are indicated by the black arrows. (**D**) DFT-LDA calculated LDOS of a 5-sGNR at energies shown in (C) (LDOS sampled at a height of 3.5 Å; above the plane of the 5-sGNR) (*26*).

sawtooth-GNRs (5-sGNRs) (Fig. 1, D and E). BRSTM imaging of 5-sGNRs unambiguously confirms the presence of five-membered rings along the cove edges of the GNRs (Fig. 1D). The absence of periodic bright spots observed in the topographic STM image of 5-sGNRs (previously attributed to the superposition of hydrogen atoms along the cove edges of sGNRs) further corroborates the structural assignment (fig. S4B) (*26*).

Scanning tunneling spectroscopy of GNRs

To experimentally determine GNR metallicity, we characterized the electronic structure of sGNRs using STM spectroscopy. Figure 2A shows a typical d*I*/d*V* point spectrum obtained on a sGNR [d*I*/d*V* spectroscopy provides a measure of the local density of states (LDOS) beneath the STM tip]. Distinctive features associated with valence band (VB) and conduction band (CB) edges can be seen at V = −1.07 ± 0.03 V (state 1) and V = 1.36 ± 0.03 V (state 3), respectively. Most prominent, however, is the sharp peak in the LDOS (state 2) that is centered near $V = 0$ (E_F) (0.02 ± 0.02 V). This peak continuously spans energies both below and above E_F, a clear signature of a gapless, metallic density of states (DOS). d*I*/d*V* imaging of the wave function of these metallic sGNR states shows a characteristic serpentine pattern that snakes back and forth across the sGNR width (Fig. 2B). The valence and conduction band edge states, by contrast, have their highest intensity along the armchair edges of the GNR (Fig. 2B), consistent with previous measurements of conventional semiconducting GNRs under similar conditions (*37*, *38*). Spectroscopic measurements were also conducted on semiconducting head-to-head and tail-to-tail sGNRs (figs. S5 to S7), which are observed to host topological homojunctions (fig. S6) and metal–semiconductor heterojunctions (fig. S7), as expected from theoretical considerations (*26*).

A similar experimental analysis was performed on the 5-sGNRs (Fig. 3A). The point spectroscopy of 5-sGNRs was seen to be quite different from that of sGNRs. Although features associated with the valence band edge (V = −1.12 ± 0.03 V, state 1) and conduction band edge (V = 1.64 ± 0.09 V, state 3) of 5-sGNRs are observed at similar energies when

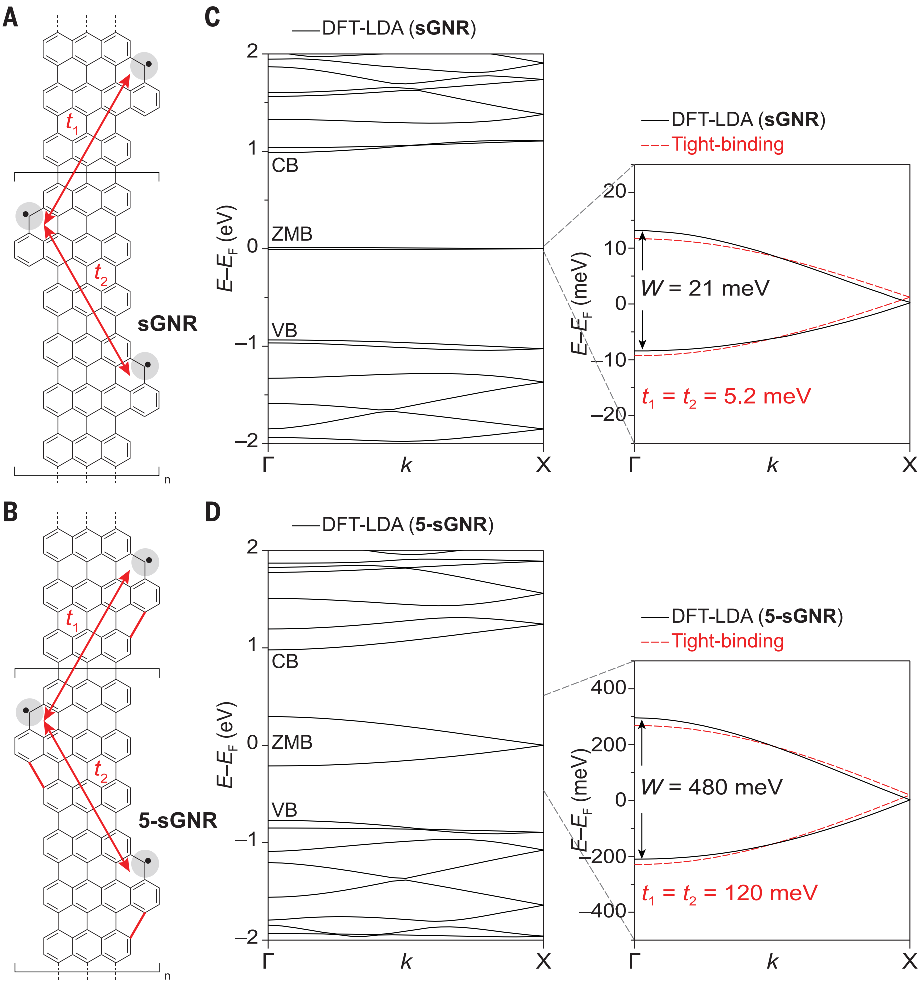

Fig. 4. Zero-mode band structure. Schematic representation of inter- and intracell hopping between localized zero modes embedded in (**A**) sGNRs and (**B**) 5-sGNRs. (**C**) Left: DFT-LDA calculated band structure for sGNRs. The valence, zero-mode, and conduction bands are labeled VB, ZMB, and CB, respectively. Right: Tight-binding fit (red) to DFT-LDA band structure yields the hopping parameter $t_1 = t_2 = 5.2$ meV. (**D**) The same as (C) but for 5-sGNRs. The hopping parameter for 5-sGNR (and corresponding bandwidth) are 23 times as large as those for sGNR (*26*).

compared to sGNR states, the spectrum of the 5-sGNR does not feature a central peak at $V = 0$ (Fig. 3A). Instead it exhibits a shallow dip at $V = 0$ and a broad DOS feature that spans an energy range above and below E_F. The electronic wave functions corresponding to states 1 to 3 in 5-sGNRs are similar to the corresponding features in sGNRs except for the lack of periodic bright spots associated with the nonplanar cove edges (Fig. 3B). For example, dI/dV images performed at biases near the conduction and valence band edges show the LDOS concentrated at the armchair edges, whereas we observe a serpentine pattern near $V = 0$ (Fig. 3B) that is very similar to the metallic state seen in sGNRs. This state can be observed in dI/dV maps as the sample bias is swept across the dip at $V = 0$ over a wide energy range (-0.46 V < V < 0.50 V) (figs. S8 and S9), including biases where the sGNR ZMB cannot be observed (fig. S10) (*26*). This implies that 5-sGNRs are also metallic and that the LDOS dip observed near $V = 0$ is not an energy gap but rather a 1D metallic DOS feature resulting from van Hove singularities (see Fig. 3C). The peaks near $V = 0$ associated with the 5-sGNR ZMB shift slightly depending on the tip position during STS experiments (fig. S8D) (*26*).

Ab initio calculations of GNR electronic structure

We further explored the apparent metallicity of sGNRs by using ab initio density functional theory (DFT). Figure 4C shows the resulting band structure calculated for an isolated sGNR by means of the local density approximation (LDA). Two narrow bands [denoted zero-mode bands (ZMBs)] are observed bracketing E_F, whereas CB and VB edges can be seen at energies much further from E_F. The two bands bracketing E_F have no bandgap and are fit well by the SSH expression (Eq. 1) with $t_1 = t_2 = 5.2$ meV and $\delta = 0$ (Fig. 4C, red dashed lines), and are also stable against Peierls distortion (*39*) (as confirmed by supercell calculations). The resulting theoretical DOS (Fig. 2C) shows a single peak centered at E_F, as well as VB and CB peaks at lower and higher energies, respectively, in good agreement with the STM point spectroscopy for sGNRs (Fig. 2A). The theoretical wave function maps (Fig. 2D) match the experimental dI/dV maps obtained at E_F and at the band edge energies, providing further evidence of metallicity in sGNRs.

Although our sGNRs clearly match the metallic predictions of the symmetric SSH model, a potential complication is the very narrow metallic sGNR bandwidth (~21 meV). Metals with a high DOS at E_F are often unstable to Mott insulator transitions or magnetic phase transitions as dictated by the Stoner criterion (*40*, *41*). The metallic behavior indicated theoretically may be caused by the spin polarization not being accounted for in our simplified tight-binding or LDA-based calculations. To test for this type of magnetic instability in sGNRs, we calculated the sGNR band structure using the local spin density approximation (LSDA) for an isolated sGNR. The result (fig. S11) shows that the sGNR electronic structure does, in fact, undergo a ferromagnetic phase transition that opens a 200-meV energy gap about E_F (*26*). We do not see a gap experimentally because of a combined effect of p-doping and surface electric fields induced by the underlying Au(111) substrate. When these are properly accounted for in our DFT calculation, the gap does, indeed, vanish at the LSDA level, and the metallic result is recovered (fig. S11D) (*26*). Therefore, although it is technically correct to say that sGNR/Au(111) is metallic, our DFT calculation predicts that a substantial energy gap will open up and metallicity will be lost owing to a magnetic phase transition as soon as this sGNR is removed from the Au(111) surface. This represents an interesting and potentially useful 1D magnetic phase transition, but the question remains whether it is possible to engineer a sGNR with more robust metallicity that would not suffer this fate.

This question can be answered by examining the 5-sGNR, whose metallic DOS features are much wider in energy than the narrow peak at E_F seen for sGNRs (Figs. 2 and 3). To clarify the robustness of 5-sGNR metallicity, we also analyzed its electronic structure through ab initio DFT calculations. At the LDA level, the 5-sGNR band structure does, indeed, show a much wider metallic band than the corresponding sGNR band structure (Fig. 4, C and D) [Perdew-Burke-Ernzerhof (PBE) functionals yield a nearly identical band structure (fig. S12)] (*26*). When the SSH expression (i.e., the tight-binding result from Eq. 1) is fit to the 5-sGNR DFT-LDA band structure, we find a hopping amplitude of $t_1 = t_2 = 120$ meV, which corresponds to a bandwidth 23 times as large as the sGNR DFT-LDA bandwidth (Fig. 4D, red dashed lines). This is also reflected in the calculated DOS (Fig. 3C), which shows a broad U-shaped feature (with peaks at the band edges characteristic of 1D van Hove singularities), consistent with the experimental minimum in dI/dV intensity observed at $V = 0$ for 5-sGNR point spectroscopy (Fig. 3A). The experimental peaks associated with the 5-sGNR van Hove singularities appear to be additionally broadened, perhaps as a result of substrate hybridization or finite quasiparticle lifetime effects. The theoretical LDOS patterns calculated for the 5-sGNR band-edge and metallic states (Fig. 3D) also correspond well to the 5-sGNR experimental dI/dV images (Fig. 3B). Our DFT calculations of the 5-sGNR at the LSDA level additionally show no signs of magnetism (with or without substrate doping) and are identical to the LDA-based results (fig. S13) (*26*). We conclude that 5-sGNRs exhibit robust metallicity with a much wider bandwidth than sGNRs, both experimentally and theoretically, and are not expected to undergo a magnetic phase transition upon transfer from Au(111) to an insulator.

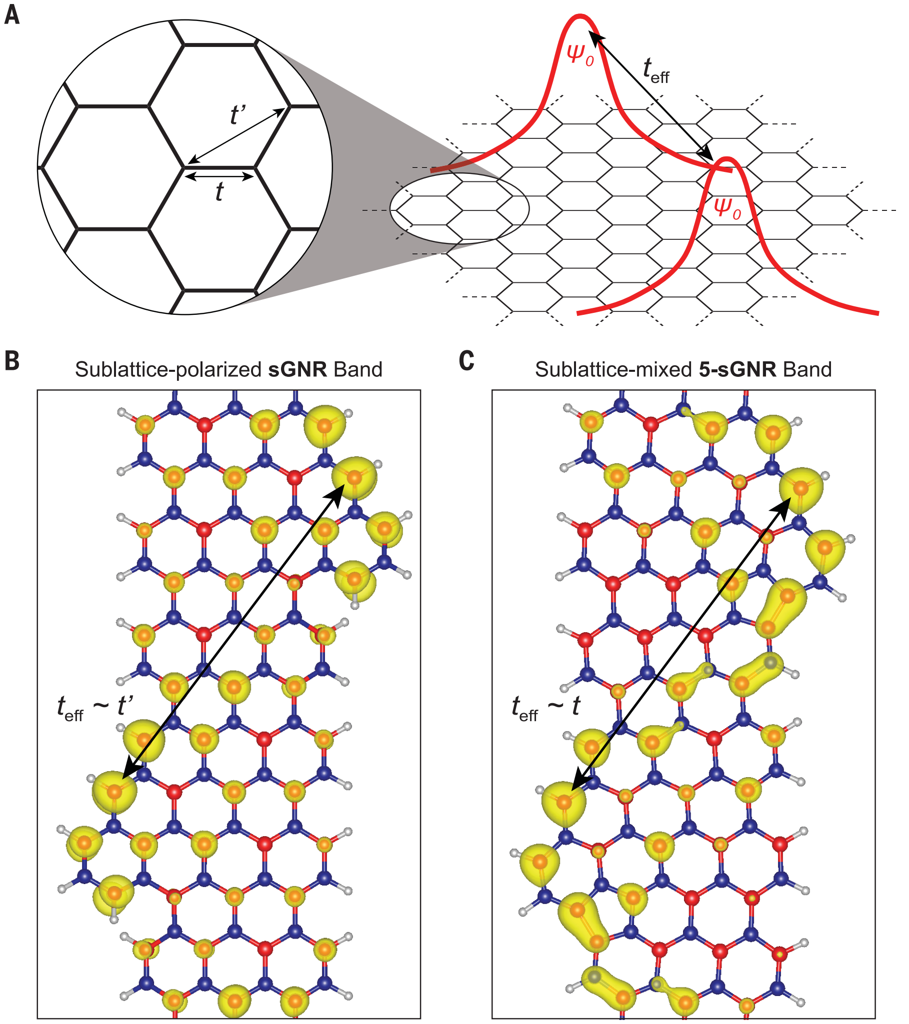

Fig. 5. Zero-mode engineering in sGNRs. (**A**) Diagram of effective hopping t_{eff} between two localized states (labeled ψ_0) embedded in graphene. Inset: Schematic representation of the first (t) and second (t') nearest-neighbor hopping parameters of graphene. (**B**) DFT-calculated wave function isosurface of a sGNR for states near $E = 0$ (5% charge density isosurface shown). (**C**) Same as (B) but for 5-sGNRs. Different sublattices are denoted with different colors (A sublattice in red and B sublattice in blue). The sGNR wave function is completely sublattice polarized, whereas the 5-sGNR wave function is sublattice mixed and more delocalized (*26*).

Discussion

How does the seemingly small structural difference between 5-sGNRs and sGNRs lead to such a large difference in their electronic behavior? The considerable increase in bandwidth observed for 5-sGNRs is a result of the loss of sublattice polarization of the ZMB electron wave functions. This sublattice mixing occurs because the graphene bipartite lattice symmetry is disrupted by the formation of five-membered rings that fuse the cove regions along the edges of sGNRs. This can be understood by remembering that the two extra atoms added to the sGNR unit cell on sublattice A result in two new localized $E = 0$ eigenstates (zero modes) per unit cell whose wave functions are also confined to sublattice A. This sublattice polarization is preserved in the sGNR Bloch waves for the two in-gap bands (Fig. 5B), and the sGNR bandwidth is determined by the effective amplitude (t_{eff}) for an electron to hop between adjacent zero modes (Fig. 5A). Because the zero modes are all on the same sublattice, it can be shown that $t_{\text{eff}} \propto t'$ where t' is the second nearest-neighbor hopping amplitude of graphene (as there is no zero-mode state density on sublattice B). In the case of 5-sGNRs, however, the bipartite lattice is disrupted by the bond that closes the coves; the zero modes are thus no longer sublattice polarized (fig. S14B) (*26*). Consequently, the resulting Bloch waves are no longer sublattice polarized [i.e., both sublattices now exhibit state density (Fig. 5C)] and so $t_{\text{eff}} \propto t$, where t is the nearest-neighbor hopping amplitude of graphene (Fig. 5A) [see (*26*) for additional details]. This explanation is consistent with the ratio of the bandwidths of the two GNRs (~23), which falls within the range of accepted values for t/t' (*42*). The key insight here is that the loss of sublattice polarization (i.e., through intentional fusion of five-membered rings along the cove edges) greatly increases the effective overlap of adjacent localized zero-mode states and strongly enhances the metallic bandwidths, even as the spatial separation between zero modes along the GNR backbone is fixed. This provides a useful design criterion for engineering robust metallic systems from zero-mode superlattices in carbon networks.

Our results provide a general strategy for introducing zero modes into graphene-based materials and reveal the important role of sublattice polarization in controlling the emergent band structure of these systems. This approach creates opportunities for developing nanoscale electrical devices and for exploring electronic and magnetic phenomena in this class of 1D metallic systems.

REFERENCES AND NOTES

1. Y.-W. Son, M. L. Cohen, S. G. Louie, *Phys. Rev. Lett.* **97**, 216803 (2006).
2. L. Yang, C.-H. Park, Y.-W. Son, M. L. Cohen, S. G. Louie, *Phys. Rev. Lett.* **99**, 186801 (2007).
3. G. E. Moore, *Proc. IEEE* **86**, 82–85 (1998).
4. M. Bockrath *et al.*, *Nature* **397**, 598–601 (1999).
5. J. Luttinger, in *Luttinger Model: The First 50 Years and Some New Directions* (World Scientific, 2014), pp. 3–11.
6. J. Voit, *Rep. Prog. Phys.* **58**, 977–1116 (1995).
7. A. R. Goñi *et al.*, *Phys. Rev. Lett.* **67**, 3298–3301 (1991).
8. H. Kataura *et al.*, *Synth. Met.* **103**, 2555–2558 (1999).
9. M. F. Lin, K. W.-K. Shung, *Phys. Rev. B Condens. Matter* **50**, 17744–17747 (1994).

10. P. Monçeau, N. Ong, A. M. Portis, A. Meerschaut, J. Rouxel, *Phys. Rev. Lett.* **37**, 602–606 (1976).
11. G. Grüner, A. Zawadowski, P. Chaikin, *Phys. Rev. Lett.* **46**, 511–515 (1981).
12. Z. K. Tang *et al.*, *Science* **292**, 2462–2465 (2001).
13. I. Takesue *et al.*, *Phys. Rev. Lett.* **96**, 057001 (2006).
14. Y.-C. Chen *et al.*, *ACS Nano* **7**, 6123–6128 (2013).
15. J. Cai *et al.*, *Nature* **466**, 470–473 (2010).
16. L. Talirz *et al.*, *ACS Nano* **11**, 1380–1388 (2017).
17. P. Ruffieux *et al.*, *Nature* **531**, 489–492 (2016).
18. D. J. Rizzo *et al.*, *Nano Lett.* **19**, 3221–3228 (2019).
19. D. J. Rizzo *et al.*, *Nature* **560**, 204–208 (2018).
20. O. Gröning *et al.*, *Nature* **560**, 209–213 (2018).
21. T. Cao, F. Zhao, S. G. Louie, *Phys. Rev. Lett.* **119**, 076401 (2017).
22. Y.-L. Lee, F. Zhao, T. Cao, J. Ihm, S. G. Louie, *Nano Lett.* **18**, 7247–7253 (2018).
23. K.-S. Lin, M.-Y. Chou, *Nano Lett.* **18**, 7254–7260 (2018).
24. J. Jiang, S. G. Louie, Topology Classification from Chiral Symmetry: Chiral Phase Index and Spin Correlations in Graphene Nanoribbons. arXiv:2002.04628 [cond-mat.mtrl-sci] (2020).
25. W. P. Su, J. R. Schrieffer, A. J. Heeger, *Phys. Rev. B Condens. Matter* **22**, 2099–2111 (1980).
26. See supplementary materials.
27. E. H. Lieb, *Phys. Rev. Lett.* **62**, 1201–1204 (1989).
28. M. M. Ugeda, I. Brihuega, F. Guinea, J. M. Gómez-Rodríguez, *Phys. Rev. Lett.* **104**, 096804 (2010).
29. M. Inui, S. A. Trugman, E. Abrahams, *Phys. Rev. B Condens. Matter* **49**, 3190–3196 (1994).
30. J. J. Palacios, J. Fernández-Rossier, L. Brey, *Phys. Rev. B Condens. Matter Mater. Phys.* **77**, 195428 (2008).
31. G. Li, K.-Y. Yoon, X. Zhong, X. Zhu, G. Dong, *Chemistry* **22**, 9116–9120 (2016).
32. W. Yang, A. Lucotti, M. Tommasini, W. A. Chalifoux, *J. Am. Chem. Soc.* **138**, 9137–9144 (2016).
33. A. Narita *et al.*, *Nat. Chem.* **6**, 126–132 (2014).
34. K.-J. Shi *et al.*, *Org. Lett.* **19**, 2801–2804 (2017).
35. C. Bronner *et al.*, *ACS Nano* **12**, 2193–2200 (2018).
36. C. Bronner *et al.*, *J. Phys. Chem. C* **121**, 18490–18495 (2017).
37. P. Ruffieux *et al.*, *ACS Nano* **6**, 6930–6935 (2012).
38. Y.-C. Chen *et al.*, *Nat. Nanotechnol.* **10**, 156–160 (2015).
39. C. Van Nguyen *et al.*, *J. Electron. Mater.* **46**, 3815–3819 (2017).
40. E. C. Stoner, *Proc. R. Soc. London Ser. A* **165**, 372–414 (1938).
41. E. C. Stoner, *Proc. R. Soc. London Ser. A* **169**, 339–371 (1939).
42. R. Kundu, *Mod. Phys. Lett. B* **25**, 163–173 (2011).
43. https://www.quantum-espresso.org/.
44. D. J. Rizzo *et al.*, Data for figures: Inducing Metallicity in Graphene Nanoribbons via Zero-Mode Superlattices, Zenodo (2020); https://doi.org/10.5281/zenodo.3940702.

ACKNOWLEDGMENTS

Funding: Research was supported by the Office of Naval Research MURI Program N00014-16-1-2921 (molecular design, STM spectroscopy, band structure); by the U.S. Department of Energy (DOE), Office of Science, Basic Energy Sciences (BES), under the Nanomachine Program award number DE-AC02-05CH11231 (surface growth, image analysis); by the Center for Energy Efficient Electronics Science NSF Award 0939514 (precursor synthesis); and by the National Science Foundation under grants DMR-1508412 (structural relaxation studies) and DMR-1926004 (LSDA simulations), as well as DMR-1839098 (zero-mode analysis). Computational resources were provided by the DOE Lawrence Berkeley National Laboratory's NERSC facility and by the NSF through XSEDE resources at NICS. **Author contributions:** D.J.R., G.V., J.J., S.G.L., M.F.C., and F.R.F. initiated and conceived the research; G.V., R.M., and F.R.F. designed, synthesized, and characterized the molecular precursors; D.J.R., C.B., T.Ch., and M.F.C. performed on-surface synthesis and STM characterization and analysis; J.J., T.Ca., and S.G.L. performed the DFT calculations and the theoretical analysis that predicted and interpreted the STM data. All authors contributed to the scientific discussion. **Competing interests:** The authors declare no competing interests. **Data and materials availability:** The DFT code and pseudopotentials can be downloaded from the Quantum Espresso website (*43*). For this study, we used version 6.3 for the theoretical calculations. All data presented in the main text and the supplementary materials can be found in the corresponding Zenodo repository (*44*).

SUPPLEMENTARY MATERIALS

science.sciencemag.org/content/369/6511/1597/suppl/DC1
Materials and Methods
Supplementary Text
Figs. S1 to S15
References (*45–50*)

12 June 2019; resubmitted 13 December 2019
Accepted 14 July 2020
10.1126/science.aay3588

Science

Inducing metallicity in graphene nanoribbons via zero-mode superlattices

Daniel J. Rizzo, Gregory Veber, Jingwei Jiang, Ryan McCurdy, Ting Cao, Christopher Bronner, Ting Chen, Steven G. Louie,
Felix R. Fischer and Michael F. Crommie

Science **369** (6511), 1597-1603.
DOI: 10.1126/science.aay3588

Making metallic ribbons

In its usual two-dimensional form, graphene does not have an energy gap in its electronic structure. However, one-dimensional ribbons made of the material are semiconducting and making them metallic is tricky. Rizzo *et al.* developed a strategy for synthesizing metallic graphene nanoribbons and demonstrated their metallicity using scanning tunneling spectroscopy. These metallic graphene nanoribbons may be useful for exploring exotic quantum phases in a single dimension.

Science, this issue p. 1597

Science (print ISSN 0036-8075; online ISSN 1095-9203) is published by the American Association for the Advancement of Science, 1200 New York Avenue NW, Washington, DC 20005. The title *Science* is a registered trademark of AAAS.